

Determination of New Zealand Ocean Bottom Seismometer Orientation via Rayleigh-Wave Polarization

by J. C. Stachnik, A. F. Sheehan, D. W. Zietlow, Z. Yang, J. Collins, and A. Ferris

Online material: Complete list of earthquakes used in this study.

INTRODUCTION

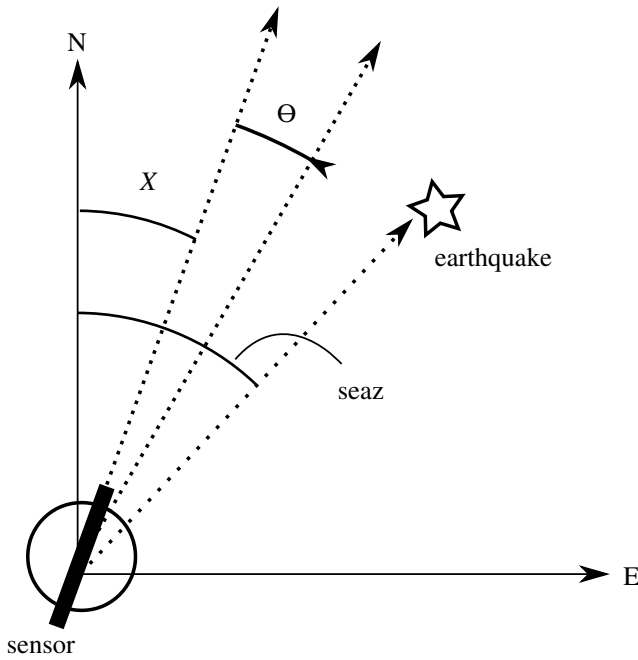
Three-component ground-motion recordings are critical to modern seismic analysis techniques such as receiver functions and body- and surface-wave polarization studies. Modern three-component seismometers typically resolve three axes of ground motion into one vertical and two orthogonal horizontal directions. The standard convention for installation is to orient the instrument such that one of the horizontal components is aligned with true north, taking into account the current local magnetic declination at the station. This practice can be difficult in the case of borehole instruments and practically impossible for ocean-bottom seismometers (OBS). Some deployments of OBS have used airgun shots to determine sensor orientation (Anderson *et al.*, 1987; Duennebieer *et al.*, 1987); however, this is not an error- or cost-free procedure and is not always available. In these cases, determination of sensor orientation is necessary independent of human interaction with the physical instrument. The elliptical particle motion of Rayleigh waves is exploited here to calculate sensor orientation based on the statistical analysis of earthquakes recorded on OBS deployed around the south island of New Zealand. This robust method is computationally fast because synthetic seismograms are not generated and accurate source parameters are not necessary. The technique is compared with body-wave orientation results and full-waveform surface-wave orientation results. Application of this method to waveforms recorded on land stations and synthetic waveforms confirms its reliability.

RAYLEIGH-WAVE POLARIZATION

Surface-wave arrival azimuth is determined via polarization analysis of the Rayleigh wave recorded on a three-component sensor. Rayleigh waves exhibit retrograde elliptical particle motion, theoretically only observed on the vertical and radial

components. Because it is more stable to quickly determine a linear relationship than to measure ellipticity, the polarization analysis is performed by cross correlating the vertical component with the Hilbert-transformed radial component. The 90° phase shift associated with the Hilbert transform yields a theoretically linear relationship between the two signals. Verticality of the Z component is fundamental to this analysis. OBS achieve this using a motor-driven gimbal, tilt sensor, and controller that bring the Z channel to vertical and level the instrument automatically if necessary. For a sensor with unknown orientation (X), the radial component is computed from the two horizontal components (e.g., BHN/BHE, or BH1/BH2) for a range of assumed back-azimuth directions (θ), assuming one of the horizontal components represents the north component. Figure 1 illustrates how the sensor orientation can be determined as $X = \text{seaz} - \theta$, where seaz is the station-to-event azimuth along the great circle path.

The polarization analysis and the equations presented here are based on surface-wave back-azimuth estimation studies for Rayleigh-wave detection (Chael, 1997; Selby, 2001; Baker and Stevens, 2004). Ekström and Busby (2008) determine station orientation by examining correlations between observed and synthetic surface-wave time series over a range of orientations. Three-component synthetic waveforms are calculated for specified source parameters and systematically compared with the observed Rayleigh wave. This approach is generally robust, but computationally intensive. The method of Baker and Stevens (2004) that we employ here uses only the polarization of observed Rayleigh-wave seismograms and does not depend on accurate source-rupture parameters. Laske *et al.* (1994) also use observed surface waves to determine orientation, utilizing a spectral eigenvalue decomposition to determine ellipticity and arrival angles for both Rayleigh and Love waves. This method provides frequency-dependent surface-wave polarization measurements based on multitaper spectral analysis of surface waves. We prefer the method of Baker and Stevens (2004) for its simplicity and computational speed.



▲ **Figure 1.** Illustration of coordinate system and terms used to define the correct seismometer orientation (X) from the observed station-to-event azimuth ($seaz$) and the calculated seaz from Rayleigh-wave polarization (\otimes), which is determined as shown in Figure 2.

The Rayleigh-wave polarization analysis is attempted for all possible earthquakes for each station, based on the National Earthquake Information Center (NEIC) catalog with body- or surface-wave magnitude greater than 6.0 during the time period of operation. This is between 31 January 2009 and 13 February 2010 for the New Zealand OBS. (For a complete list of earthquakes, see [Table S1](#) in the electronic supplement to this article.) The Rayleigh-wave time windows used for analysis were taken from 20 s before a predicted 4.0-km/s phase arrival to 600 s after it. The waveform window was tapered with a 10% cosine taper, then band-pass Butterworth filtered from 0.02 to 0.04 Hz (50 to 25 s; Fig. 2a).

Next, the radial component is computed for a range of back azimuths (θ in Fig. 1). Figure 2b shows the envelope of the computed radial component for back azimuths from 0° to 360° . Analysis of a single earthquake is shown in Figure 2.

To assess the relationship between the Hilbert-transformed vertical component and the radial component, the zero-lag cross correlation is calculated by

$$S_{jk} = \sum_{\tau=1}^N x_j(\tau)x_k(\tau), \quad (1)$$

where $j, k = z$ (vertical) or \bar{r} (radial), and $x_z(\tau)$, $x_{\bar{r}}(\tau)$ are the vertical and Hilbert-transformed horizontal signals, respectively. To expedite processing, the Hilbert transform of the vertical component is correlated with the computed radial component for each θ .

A normalized cross correlation is computed to assess the linearity between these two signals:

$$C_{z\bar{r}} = \frac{S_{z\bar{r}}}{\sqrt{S_{zz}S_{\bar{r}\bar{r}}}}. \quad (2)$$

This function is useful because it is bounded on the interval -1 to 1 (Fig. 2c, dashed line), but it is difficult to find a maximum because the autocorrelation of the radial component ($S_{\bar{r}\bar{r}}$) in the denominator varies with the numerator. This can result in a range of back azimuths with similar values near the maximum. Thus a second normalization is used:

$$C_{z\bar{r}}^* = \frac{S_{z\bar{r}}}{S_{zz}}, \quad (3)$$

which has a well-defined maximum value and is used to select the appropriate azimuth (Fig. 2c, solid line). However, this value is unbounded and not used when assessing the quality of the cross correlation (i.e., $C_{z\bar{r}}$ is used for data culling and is shown in Fig. 3c instead of $C_{z\bar{r}}^*$).

Varying the range of back azimuth from 0° to 360° to calculate the correlation coefficient is useful here to resolve the 180° ambiguity discrepancy found in body-wave analysis. With the assumption that the Rayleigh wave exhibits retrograde elliptical particle motion, the maximum positive correlation coefficient indicates the azimuth of maximum correlation between the vertical and Hilbert-transformed radial component (Fig. 2c). Conversely, the maximum negative correlation coefficient is 180° away. Observations of prograde particle motion are rare (Tanimoto and Rivera, 2005) and would be evident in the envelope of the radial components.

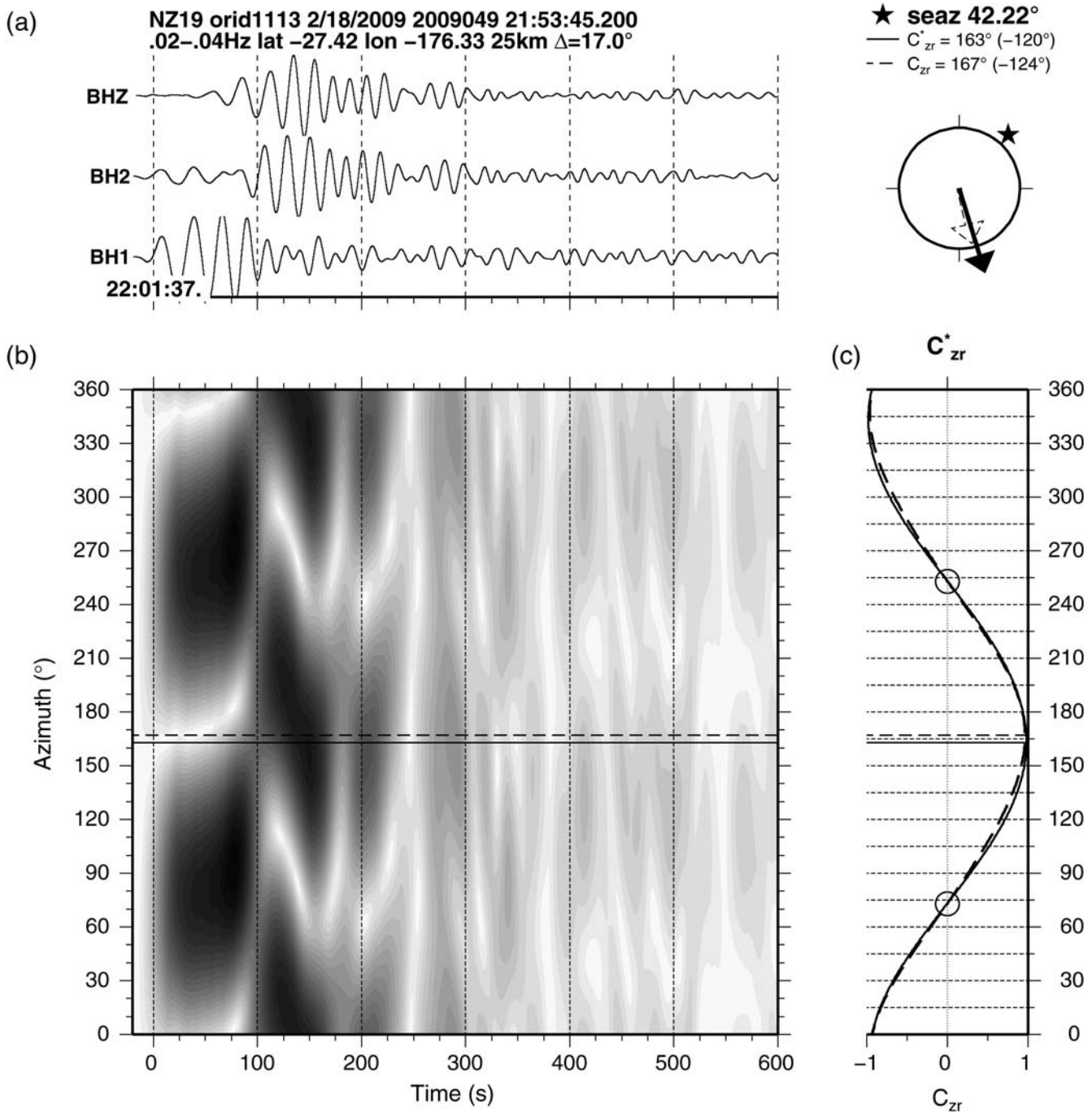
DATA CULLING

Propagation effects such as near-station scattering can lead to surface-wave arrivals that are off the great circle path between the source and receiver. This causes variability in the data, even for correctly oriented sensors, so culling of the data is necessary based on several criteria. Three standard statistics, circular mean of the azimuth residual $\bar{\phi}$, 95% confidence of the mean, and circular median of the azimuth residual ϕ_m were used to assess the data (Berens, 2009). In addition, three culling procedures (Fig. 3) were used to determine the final set of sensor orientations:

- C1—Calculate circular mean, and retain observations within 95% confidence interval.
- C2—Use data from earthquakes with depth < 100 km, and keep observations $C_{z\bar{r}}^* > 0.4$.
- C3—C2 then C1 culling.

Because the mean value can be biased by outliers, the median absolute deviation (MAD, which is the median of the absolute deviations from the data's median; Mosteller and Tukey, 1977) is also calculated by

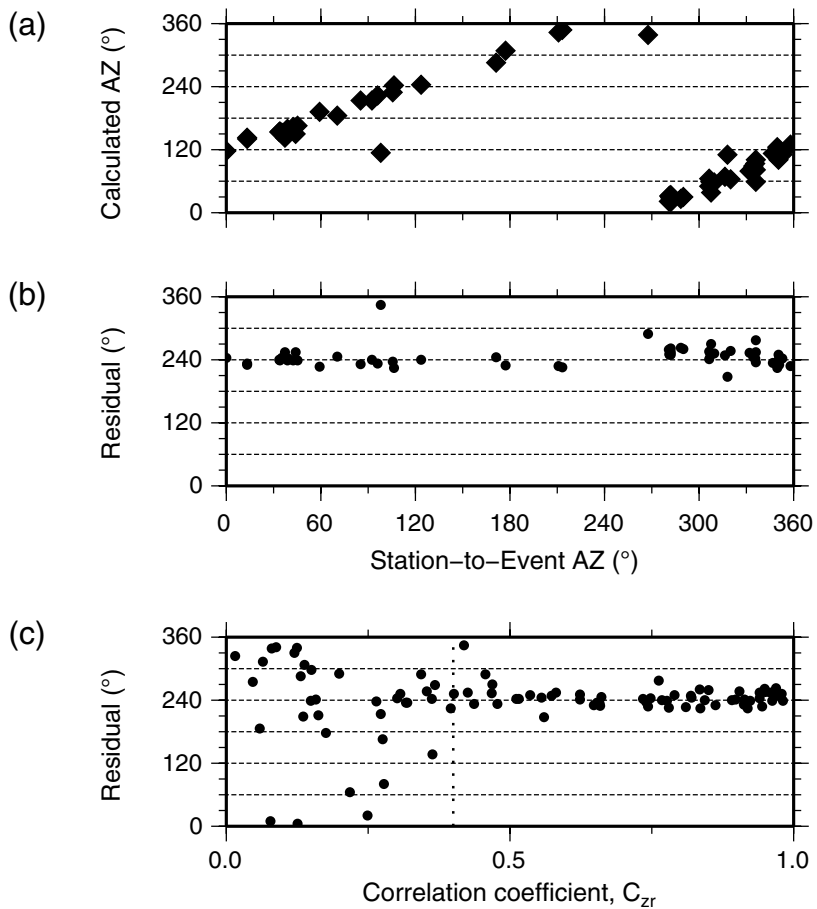
$$MAD = \text{median}_i(|X_i - \text{median}_j(X_j)|). \quad (4)$$



▲ Figure 2. Surface-wave polarization analysis for an earthquake recorded on station NZ19. The upper right corner shows a summary of the analysis; seaz is the great-circle arc azimuth from station to epicenter, and values in parentheses are residuals. (a) Windowed three-component surface waves for event parameters are as indicated, filtered with a band pass of 0.02–0.04 Hz. Note the strong Love-wave arrival on the BH1 component in (a) does not bias the determination of the appropriate Rayleigh-wave arrival angle. (b) Image of the envelope of the radial component computed at the range of back azimuths indicated along the y-axis, assuming BH2 is the north component. (The gray scale is normalized 0/1, and darker colors represent higher amplitudes.) (c) Correlation coefficient as a function of back azimuth: dashed line, C_{zr} , equation (2); solid line, C_{zr}^* , equation (3); circles, zero crossings for C_{zr}^* .

This value can be scaled such that it is equal to the standard deviation for a Gaussian distribution, $\hat{\sigma}(\text{SMAD}) = K \times \text{MAD}$, where K varies with the type of distribution. For normal, Gaussian-distributed data, $\text{SMAD} = 1.4826 \times \text{MAD}$ (Rousseeuw and Croux, 1983).

The most robust value for sensor orientation is the median value after C3 culling. The table summary shown in Figure 3 shows that the median value does not change from the raw residuals to the final C3 culling; however, the deviation from the median (SMAD) significantly decreases as expected.



NZ19

	Mean (95%)	Med (SMAD)	N
Raw:	249.4°(9.9°)	243.2°(21.1°)	113
C1:	248.3°(1.9°)	248.8°(7.9°)	36
C2:	245.0°(4.9°)	242.8°(14.2°)	57
C3:	244.6°(1.6°)	243.2°(3.3°)	17

▲ **Figure 3.** Summary of results for all earthquakes processed at station NZ19 in the frequency band 0.02–0.04 Hz. The upper right corner shows a summary of observations and culling statistics. See Data Culling for C1, C2, and C3 culling parameters. Data shown in (a–c) represent back-azimuth determination from the C_{zr}^* correlation coefficient after C2 culling. (a) Calculated back azimuth as a function of great-circle arc station-to-event azimuth. (b) Back-azimuth residual as a function of great circle-arc station-to-event azimuth. (c) Back-azimuth residual as a function of correlation coefficient C_{zr} . Vertical dashed line shows minimum correlation coefficient cutoff value for culling C2 and C3. (d) Polar histogram representation of back-azimuth residuals. Mean value from C2 culling indicated by black arrow.

RESULTS

Results from determining the sensor orientation of 30 OBS stations and 4 land stations deployed around the South Island of New Zealand are presented in Table 1. Results are presented for both the C2 and C3 culling described previously (see Data Culling). In general, the median azimuth of the north component from surface-wave analysis does not vary significantly between these culling steps, although the associated error diminishes.

CONFIDENCE TESTING

Two confidence tests were performed to investigate the robustness of this method for determining seismometer orientation from Rayleigh-wave polarization. The first test consisted of calculating zero-noise surface-wave synthetic waveforms via the Mineos software (Masters *et al.*, 2011) using a one-dimensional

preliminary reference Earth model (PREM) velocity model. Synthetic waveforms were calculated for real station locations of the Global Seismic Network (GSN) and a known earthquake location taken from the Preliminary Determination of Epicenters (PDE) catalog. All examples confidently recover the appropriate station-to-event azimuth using the C_{zr}^* correlation coefficient. Figure 4 illustrates this analysis for synthetic waveforms calculated for the GSN station BILL. As Baker and Stevens (2004) point out, C_{zr} does not perform correctly in these noise-free synthetic cases (Fig. 4c, dashed line).

Rayleigh-wave polarization analysis was also performed on U.S. network station MVCO. According to the results of Ekström and Busby (2008), the north component of this station is pointed to an azimuth of approximately 19° E. In addition, metadata archived from the Incorporated Research Institutions for Seismology Data Management Center (IRIS-DMC) reports a misorientation of 18.5° E. The method described here was applied to 121 earthquakes recorded between 1 January

TABLE 1
Summary of Analysis for 0.02–0.04 Hz Filter Band, with Results for C2 and C3 Culling of the Surface-Wave Analysis, Along with Body-Wave (BW) Analysis Results

Station		$\bar{\phi}$	95% Confidence	ϕ_m	SMAD	N
CASS	C2	1.3	3.3	1.2	0.6	52
	C3	1.0	1.4	1.2	0.6	10
	BW	4.4	5.9	5.0	4.4	7
CROE	C2	4.7	4.9	4.1	0.9	49
	C3	4.8	1.8	4.3	5.0	13
	BW	359.8	12.8	4.5	0.7	6
FREW	C2	2.6	3.2	3.2	2.1	69
	C3	2.5	0.8	3.0	1.9	15
	BW	4.0	6.7	0.0	0.0	9
KELY	C2	0.6	4.0	1.2	0.7	61
	C3	0.8	1.1	0.8	0.3	22
	BW	3.3	27.7	2.0	0.0	10
NZ02	C2	36.6	7.3	36.1	11.6	47
	C3	36.4	2.4	36.3	8.0	18
	BW	39.0	23.5	30.0	5.9	11
NZ03	C2	292.9	3.6	292.2	9.8	79
	C3	292.7	0.9	292.5	2.7	25
	BW	286	5.4	283	3.0	11
NZ04	C2	206.2	3.0	204.6	7.9	79
	C3	205.9	0.6	205.7	1.6	21
	BW	199.5	3.4	198.0	4.4	11
NZ05	C2	264.9	4.4	262.7	11.4	68
	C3	264.6	1.1	264.3	3.3	25
	BW	258.6	26.0	260.0	11.9	11
NZ06	C2	197.1	3.9	197.7	13.6	58
	C3	197.3	1.3	197.5	2.8	12
	BW	205.4	17.2	202.0	4.4	11
NZ07	C2	88.8	8.9	89.0	12.3	35
	C3	87.9	2.3	89.0	5.2	17
	BW	74.7	NA	91.0	8.9	11
NZ08	C2	356.1	5.0	355.3	1.2	51
	C3	355.8	1.7	355.3	1.2	13
	BW	3.9	27.6	357.0	1.5	11
NZ09	C2	316.0	3.7	314.0	13.0	70
	C3	315.8	1.2	315.3	1.9	14
	BW	309.1	24.5	315.0	10.4	11
NZ10	C2	39.1	4.6	40.6	11.4	58
	C3	40.5	1.0	40.6	1.5	18
	BW	36.9	4.2	35.0	4.4	11
NZ11	C2	173.2	3.1	174.9	11.0	63
	C3	173.7	1.1	174.5	1.8	13
	BW	161.4	5.1	166.0	3.0	11

Mean ($\bar{\phi}$), median (ϕ_m), and other statistics are described in the text (see Data Culling).
(Continued next page.)

TABLE 1 (Continued)
Summary of Analysis for 0.02–0.04 Hz Filter Band, with Results for C2 and C3 Culling of the Surface-Wave Analysis, Along with Body-Wave (BW) Analysis Results

Station		$\bar{\phi}$	95% Confidence	ϕ_m	SMAD	N
NZ12	C2	117.2	7.8	117.0	9.9	34
	C3	115.6	2.0	116.4	6.4	20
	BW	130.2	NA	115.0	41.5	11
NZ13	C2	94.9	5.3	91.6	13.2	60
	C3	94.5	1.9	93.0	4.2	15
	BW	88.2	5.1	86.0	4.4	11
NZ14	C2	345.8	3.8	344.3	9.3	57
	C3	346.1	1.6	346.5	3.9	11
	BW	338.2	37.1	334.0	3.0	11
NZ15	C2	250.2	8.0	250.8	12.6	16
	C3	248.2	4.1	249.5	7.0	7
	BW	243.4	NA	246.0	10.4	11
NZ16	C2	54.1	3.8	53.3	13.9	67
	C3	54.2	0.9	54.8	1.8	17
	BW	52.7	22.7	49.0	3.0	11
NZ18	C2	321.2	4.1	322.3	11.4	61
	C3	321.8	1.0	321.7	2.4	18
	BW	322.6	22.6	321.0	8.9	11
NZ19	C2	245.0	4.9	242.8	14.2	57
	C3	244.6	1.6	243.2	3.3	17
	BW	234.3	25.3	234.0	20.8	11
NZ20	C2	155.5	2.7	153.8	10.1	61
	C3	155	0.9	154.2	1.8	16
	BW	155.7	24.4	152.0	3.0	11
NZ21	C2	239.0	4.7	237.7	11.7	45
	C3	237.9	1.5	237.7	3.1	12
	BW	227.6	39.1	243.0	23.7	11
NZ22	C2	233.8	6.8	235.5	17.8	53
	C3	234	1.8	233.5	5.5	20
	BW	235.2	24.8	238.0	13.3	11
NZ23	C2	13.1	3.9	13.6	11.9	54
	C3	13.6	1.3	13.6	3.4	14
	BW	9.4	38.3	8.0	1.5	11
NZ24	C2	283.6	5.8	282.9	12.9	62
	C3	283.7	1.7	283.0	5.9	23
	BW	285.6	5.1	287.0	8.9	11
NZ25	C2	38.6	9.2	35.5	12.5	65
	C3	37.2	1.6	36.6	5.5	31
	BW	30.2	5.0	31.0	7.4	11
NZ26	C2	109.9	4.8	106.4	10.4	62
	C3	109.5	1.3	108.8	3.6	19
	BW	107.2	6.1	109.0	10.4	11

Mean ($\bar{\phi}$), median (ϕ_m), and other statistics are described in the text (see Data Culling).
(Continued next page.)

TABLE 1 (Continued)
Summary of Analysis for 0.02–0.04 Hz Filter Band, with Results for C2 and C3 Culling of the Surface-Wave Analysis, Along with Body-Wave (BW) Analysis Results

Station		$\bar{\phi}$	95% Confidence	ϕ_m	SMAD	N
NZ27	C2	218.1	4.8	214.7	7.7	59
	C3	216.8	0.9	216.8	2.2	20
	BW	215.1	25.5	211.0	3.0	11
NZ28	C2	329.5	5.2	328.4	11.4	46
	C3	329.4	1.8	330.1	4.4	14
	BW	319.3	18.1	321.0	8.9	11
NZ29	C2	44.7	4.8	44.5	14.1	61
	C3	44.2	1.9	43.9	3.0	11
	BW	48.7	16.9	44.0	10.4	11
NZ30	C2	56.5	5.9	56.3	15.3	67
	C3	56.7	1.7	57.4	4.3	17
	BW	54.5	26.3	58.0	8.9	11

Mean ($\bar{\phi}$), median (ϕ_m), and other statistics are described in the text (see Data Culling).

2010 and 31 December 2010 at MVCO. We determine a sensor misorientation of $20.1^\circ (+/- 2.5^\circ)$ E. It is important to note that the orientation anomaly angles reported by Ekström and Busby (2008) are relative to the sensor component azimuth given in the station metadata.

P-Wave Analysis

In addition to the Rayleigh-wave polarization analysis described previously in this article, we also analyze body waves to obtain the horizontal component orientations of the OBS sensors. For a correctly oriented seismic sensor and assuming no anisotropic media along the ray paths, the amplitude of a direct *P*-wave arrival on the transverse (*T*) component is near zero; however, an improperly oriented sensor yields a nonzero *P*-wave amplitude on the *T* component. We performed a grid search over the orientation angle (ranging from 0° to 180° clockwise from north) to determine the orientation by identifying the maximum amplitude ratio of the *P* wave on the *R* component to that on the *T* component. We also cross correlate the resulting radial components with the vertical component to resolve the 180° ambiguity from the grid search because only a half-space (0° – 180°) is utilized.

In the body-wave analysis, a total of 11 teleseismic events (see Table S1 in the electronic supplement to this article) with epicentral distances ranging from 30° to 90° and from various back azimuths were used. The utilized time windows were selected by hand. The waveforms are band-pass filtered from 0.04 to 0.1 Hz after removal of the mean and trend. Figure 5 demonstrates the agreement between the median sensor orientations with SMAD errors determined by the Rayleigh-wave analysis and *P*-wave amplitude ratio. On average, a factor of 5 more events were utilized for the surface-wave method than for the body-wave method, in large part because of the superior signal-to-noise ratio for surface-wave arrivals than for

body-wave arrivals on OBS. The results from the body-wave analysis are also summarized in Table 1.

CONCLUSIONS

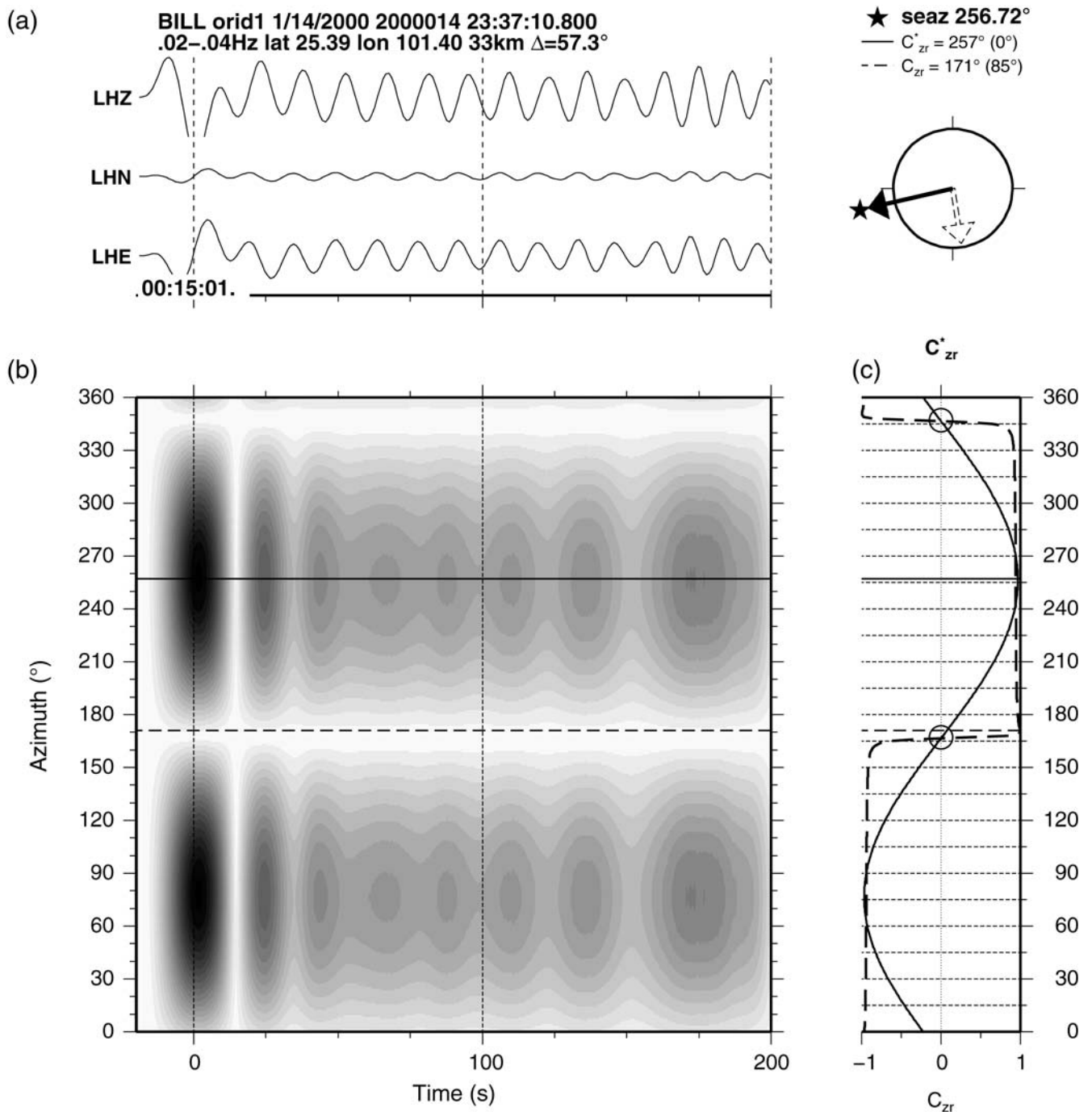
A robust method of determining Rayleigh-wave arrival azimuth has been applied to earthquakes recorded on ocean-bottom seismic stations deployed in the Pacific Ocean and Tasman Sea near New Zealand. This application allows the rapid and confident determination of the seismometer orientation once it finally rests on the seafloor. The method compares favorably with more computationally intensive surface-wave methods and with standard body-wave methods.

Discussion and Future Work

More advanced waveform windowing could be used to better isolate the Rayleigh wave. This could include computing a time window based on group velocities from global surface-wave maps. Another possibility is to detect dispersion within a larger time window and then perform the polarization analysis on a smaller window based on frequency band and signal-to-noise ratio of this dispersive wave packet. Analysis of regional events as well as teleseismic earthquakes may also prove useful.

As noted by Wang *et al.* (2006), the zero crossing of $C_{z\bar{r}}^*$ is 90° off from the maximum value and represents the azimuth at which Love-wave energy is maximized. This zero crossing is consistent between $C_{z\bar{r}}^*$ and $C_{z\bar{r}}$ and could also be used as a metric for determining the appropriate back azimuth if the maximum of $C_{z\bar{r}}^*$ is below a given threshold.

The sensor orientation can also be time dependent if the seismometer is replaced, serviced, or moved for any reason. This adds complexity to our analysis but would possibly be apparent as multimodal residuals in Figure 2b. In this case, the azimuth residual would have to be determined as a function of time. Figure 6 shows the azimuth residuals for New Zealand

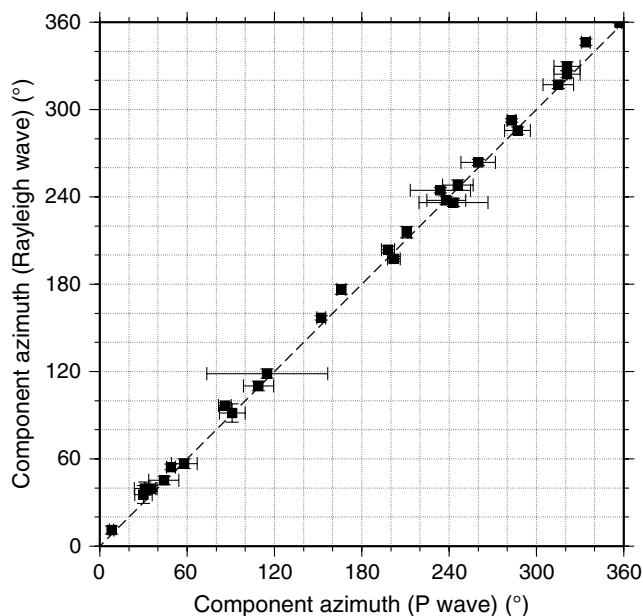


▲ **Figure 4.** Rayleigh-wave polarization analysis on noise-free synthetic waveforms in the 0.02–0.04-Hz frequency band for the GSN station BILL and the earthquake location parameters indicated. The synthetic waveforms were calculated for a station-to-event azimuth of 257°, which was determined by this method within 0.3°. Descriptions of (a–c) are similar to that in Figure 2.

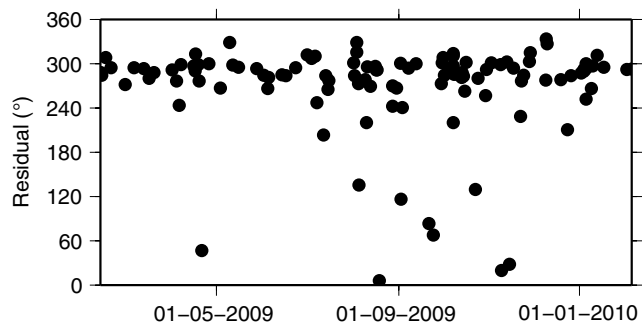
OBS station NZ03 as a function of time. As expected, this sensor resting on the seafloor does not change its orientation over the time of its deployment apart from fluctuation of measurements due to local scattering.

As evident in Figure 3, the azimuthal distribution of earthquakes relative to a station is not uniform. This may bias the determination of the sensor orientation in the presence of

tectonic structures (e.g., subducting slabs) that cause surface waves arriving from a particular azimuth range to be faster or slower. Additional bias may arise from the assumption that surface waves travel exactly along the great circle path between source and receiver. The extensive data culling used in this study alleviates much of this possible bias. Calculating the median sensor orientation for a varying range of earthquake back



▲ **Figure 5.** Comparison of sensor misorientation values determined by *P*-wave amplitude ratio with those determined by Rayleigh-wave polarization analysis. Values reported here are the median value with SMAD errors and represent the azimuth to which the BH2 component is pointing instead of true north.



▲ **Figure 6.** Rayleigh-wave arrival residual as a function of time for station NZ03. All raw residuals are shown for frequency band 0.02–0.04 Hz. Dates are in the format dd/mm/yyyy.

azimuths indicates that no systematic bias is observed with this network of stations. This is confirmed by the strong agreement with the results from body-wave analysis described previously in this article.

Shear-wave anisotropy and frequency dependence can also affect observed Rayleigh-wave polarization. Because Rayleigh waves are most sensitive to shear-velocity variations with depth, shear-wave azimuthal anisotropy of the lithosphere would be evident in Figure 3a,b as a functional variation in orientation residual with earthquake back azimuth (Smith and Dahlen, 1973). This effect could be frequency

dependent as well. The polarization analysis was also performed in the frequency band 0.04–0.06 Hz with no appreciable difference in median sensor orientation angle from 0.02–0.04 Hz.

Mismeasurement of Rayleigh-wave arrival azimuth can possibly be caused by the presence of Rayleigh-polarized microseismic noise (ambient noise) of similar amplitude and greater cross correlation than the earthquake signal. Surface-wave magnitude M_s is typically measured in the 18–22-s band. Therefore, if the microseismic noise is high in this band, relative to the earthquake, the M_s measurement could also be inaccurate. It may be possible to use noise at stations to calibrate M_s measurements. ☒

ACKNOWLEDGMENTS

We thank Peter Molnar, Craig Jones, and Gabi Laske for helpful discussions. We thank captain and crew of the R/V Thomas G. Thompson (cruise TN229) in 2009, of the R/V Roger Revelle (cruise RR1002) in 2010, and the Scripps Institution of Oceanography Ocean Bottom Seismic Instrumentation Pool (OBSIP) facility for expert assistance at sea. The instruments used in this field program were provided by the U.S. National Ocean Bottom Seismic Instrumentation Pool (<http://www.obsip.org>). Seismic data are archived at the IRIS Data Management Center. The collection of seismic data was funded by the National Science Foundation under grants EAR-0409564, EAR-0409609, and EAR-0409835. J. Stachnik was funded by the Cooperative Institute for Research in Environmental Sciences (CIRES) postdoctoral fellowship program. The authors also thank *Seismological Research Letters* editor Jonathan Lees and reviewer Neil Selby for constructive comments.

REFERENCES

- Anderson, P., F. Duennebie, and R. Cessaro (1987). Ocean borehole horizontal seismic sensor orientation determined from explosive charges, *J. Geophys. Res.* **92**, 3573–3579, doi 10.1029/JB092iB05p03573.
- Baker, G. E., and J. L. Stevens (2004). Backazimuth estimation reliability using surface wave polarization, *Geophys. Res. Lett.* **31**, no. L09611, 4 pp., doi 10.1029/2004GL019510.
- Berens, P. (2009). CircStat: A MATLAB toolbox for circular statistics, *J. Stat. Software* **31**, no. 10, 21 pp.
- Chael, E. P. (1997). An automated Rayleigh-wave detection algorithm, *Bull. Seismol. Soc. Am.* **87**, no. 1, 157–163.
- Duennebie, E., P. Anderson, and G. Fryer (1987). Azimuth determination of and from horizontal ocean bottom seismic sensors, *J. Geophys. Res.* **92**, 3567–3572, doi 10.1029/JB092iB05p03567.
- Ekström, G., and R. W. Busby (2008). Measurements of seismometer orientation at USArray Transportable Array and Backbone stations, *Seismol. Res. Lett.* **79**, no. 4, 554–561, doi 10.1785/gssrl.79.4.554.
- Laske, G., G. Masters, and W. Zurn (1994). Frequency-dependent polarization measurements of long-period surface waves and their implications for global phase-velocity maps, *Phys. Earth Planet. In.* **84**, 111–137.
- Masters, G., M. Barmine, and S. Kientz (2011). *Mineos Version 1.0.2 User Manual*, CIG/CIT, Pasadena, California, USA, 97 pp.

- Mosteller, F., and J. Tukey (1977). *Data Analysis and Regression*, Addison-Wesley, Upper Saddle River, New Jersey, 588 pp.
- Rousseeuw, P. J., and C. Croux (1983). Alternatives to the median absolute deviation, *J. Am. Stat. Assoc.* **88**, no. 424, 1273–1283.
- Selby, N. D. (2001). Association of Rayleigh waves using backazimuth measurements: Application to test ban verification, *Bull. Seismol. Soc. Am.* **91**, no. 3, 580–593.
- Smith, M., and F. Dahlen (1973). Azimuthal dependence of Love and Rayleigh-wave propagation in a slightly anisotropic medium, *J. Geophys. Res.* **78**, 3321–3333.
- Tanimoto, T., and L. Rivera (2005). Prograde Rayleigh wave particle motion, *Geophys. J. Int.* **162**, 399–405.
- Wang, G.-Q., G.-Q. Tang, D. M. Boore, G. V. N. Burbach, C. R. Jackson, X.-Y. Zhou, and Q.-L. Lin (2006). Surface waves in the western Taiwan coastal plain from an aftershock of the 1999 Chi-Chi, Taiwan, earthquake, *Bull. Seismol. Soc. Am.* **96**, no. 3, 821–845.

*J. C. Stachnik*¹

A. F. Sheehan

D. W. Zietlow

Z. Yang

Cooperative Institute for Research in Environmental Sciences

University of Colorado

Boulder, Colorado

jcstachnik@gmail.com

Department of Geological Sciences

University of Colorado

Boulder, Colorado

J. Collins

Department of Geosciences

Woods Hole Oceanographic Institute

Woods Hole, Massachusetts

A. Ferris

Weston Geophysical Corporation

Lexington, Massachusetts

¹ Now at the Geophysical Institute, University of Alaska Fairbanks, Fairbanks, Alaska.